Hindawi
Advances in Materials Science and Engineering
Volume 2021, Article ID 5884308, 9 pages
https://doi.org/10.1155/2021/5884308

Research Article

Effect of Drying Temperature on the Magnetic and Microstructural Properties of $BaFe_{12}O_{19}$ Synthesized by Coprecipitation Method

Mamman Nur Sanda,[1] **Mohsen Hakimi**,[1] **Mohamad Reza Samadzadeh Yazdi**,[2] **and Hanieh Karimi**[1]

[1]*Department of Physics, Solid State Physics, Yazd University, Research and Technology of Magnetism Lab, Yazd, Iran*
[2]*Mining and Metallurgical Engineering Department, Yazd University, Yazd, Iran*

Correspondence should be addressed to Mamman Nur Sanda; mammannur10@gmail.com

Received 19 May 2021; Revised 24 July 2021; Accepted 29 July 2021; Published 21 August 2021

Academic Editor: Ștefan Țălu

Barium hexaferrite ($BaFe_{12}O_{19}$) has dominated many aspects of technology, serving as a permanent magnet, magnetoelectric, multiferroic, and electric motors, generators, microwave devices, and drug delivery systems. There is a challenge in the synthesis of $BaFe_{12}O_{19}$ with the coprecipitation method. As a result, research is conducted to examine the factors influencing the properties of $BaFe_{12}O_{19}$ during the preparation process, specifically on the drying temperature of the mixture. The precursors were precipitated, through some procedural steps, along with stirring at 450 rpm at a certain temperature for a while and simultaneously pouring the precipitant dropwise; the sample was dried at different temperatures. The final samples were annealed at the same rate of temperature within the same time interval. The results depicted that drying at different temperatures leads to the variation in the magnetic and microstructural properties of $BaFe_{12}O_{19}$, indicating that drying at high temperatures resulted in high coercivity with low saturated magnetization.

1. Introduction

$BaFe_{12}O_{19}$ is applied to various innovative instrumental techniques for past, present, and futuristic usage. It is complex to identify any technology without detecting ferrite. $BaFe_{12}O_{19}$ has long been considered by industries due to its versatile applications, reliability, temperature stability, and as low price constituent. The availability of the constituent elements of this compound has caused the majority of the magnetic market to $BaFe_{12}O_{19}$; see [1–6].

$BaFe_{12}O_{19}$ has a hexagonal crystal structure, belonging to the magnetoplumbite crystal containing "R" block ($(BaFe_6O_{11})^{2-}$) and a cubic "S" block ($(Fe_6O_8)^{2+}$) in c-direction. When these blocks are rotated by 180°, they will be denoted by S^* and R^* with a constitutional unit cell (SG: P63/mmc, $a = 0.588$ nm, $c = 2.318$ nm). The preferred axis is c-direction where all loose crystals can easily align along the c-axis parallel to the magnetic field. Magnetic properties of different aligned directions are different, and as a result, magnetocrystalline anisotropy plays a major role in the transition of the domain wall which could enable determining the precise magnetic properties of the compound [7].

In addition, Ba^{2+} is an interruption in the crystal structure that is used to create contamination in the crystal lattice in order to keep the magnetic dipole moment in a specific direction; as a result, anisotropy is introduced. This is a natural occurrence. However, additional substances like Al, Cu, Tn, and Zn ions, are often and deliberately substituted to improve the magnetic properties. This could alter the microstructure of the material, influencing the magnetic properties as well as the mechanisms for forming the domain wall and the domain wall's motion as whole [7].

Various methods were used for $BaFe_{12}O_{19}$ synthesis, including sol-gel technique, glass crystallization, microemulsion, hydrothermal method, and the coprecipitation

method [8]. The coprecipitation method is the best and most appealing due to simplicity in the operation by comparison with the others [4].

However, there have been many attempts to explore some abnormalities that impacted on the properties of $BaFe_{12}O_{19}$ by a coprecipitation method. The effects of calcination temperature and the addition of Co on the properties of $BaFe_{12}O_{19}$ have been studied by Hajanbar et al. [9], finding that crystalline phase growth is more evident with increasing annealing temperature. The magnetic property similarly decreases when Co is dopped. As the $BaFe_{12}O_{19}$ phase grew, the coercivity is effectively reduced due to temperature dependence on magnetocrystalline anisotropy. Mosleh et al. [10] also investigated the effect of annealing temperature, which was thoroughly examined to finally discover that annealing between 90 and 500°C resulted in superparamagnetic properties, and it was simultaneously demonstrated that, with increasing temperature, the coercivity also increases until maximum coercivity and saturated magnetization are obtained at 900°C. It is also clear that the coercivity increases with particle size. Yesano and Phokha [11] indicated that pH has an effect on $BaFe_{12}O_{19}$ properties. However, the SEM images are recognized as nanorods when the annealing temperature is between 800 and 1000°C. However, in comparison to this finding [9, 10], the coercivity is unexpectedly inverted. The irregularities are limited to the effects of annealing temperature and pH values, as discovered by Balamurugun et al. [12], who provided the research with an excellent investigation on the influence of various precipitants. Among all the precipitants, two of these, NaOH and Na_2CO_3, were ultimately found to be almost shown in the single phase $BaFe_{12}O_{19}$.

Furthermore, to highlight other factors affecting the properties of $BaFe_{12}O_{19}$ with coprecipitation method is tremendously important. As a result, this study is largely dependent on the coprecipitation method. Coprecipitation is simply precipitation of a suitable substance in the mixture of two or more compounds. There are some stages along the way that involve the controlling temperature during the mixing process with a magnetic stirrer, as well as the temperature used in drying the sample after precipitation. The drying temperature is the most significant concept for achieving high magnetic properties.

This effect has received little attention. It must be treated with caution because the coprecipitation method used to synthesize $BaFe_{12}O_{19}$ nanoparticles resulted in the formation of two distinct crystalline phases. The drying temperature of the sample before final sintering influenced the crystalline phase state by adjusting the lattice parameters. By varying the drying temperature, the adherence of the two phases due to interaction reveals different results.

This paper mainly investigates the effect of drying temperature on the magnetic and microstructural properties of $BaFe_{12}O_{19}$. This is due to the availability of numerous research articles demonstrating the influence of annealing at higher temperatures, the impact of changing pH values, and the effect of various precipitants among others. Nevertheless, no effort was made to regulate the drying temperature.

The following is how the remaining sections are organized: Section 2 provides the Experimental Method, whereas Section 3 has the Results and Discussion, which includes X-ray diffraction, calculation of crystallite size and strain, magnetic properties, and morphology. The last section includes conclusion describing the clear prediction of the future endeavor.

2. Experimental Method

The coprecipitation method was used to synthesize barium hexaferrite nanoparticles. The stoichiometric amounts of high purity ferric chloride hexahydrate ($FeCl_3.6H_2O$) and barium chloride hexahydrate ($BaCl_2.6H_2O$) were dissolved in distilled water and stirred for 30 minutes at 450 rpm at the temperature of 80°C. After that, ammonia was slowly and dropwise applied to the stirring solution, until the pH reached 9. Finally, the precipitated samples were washed three times with distilled water and were divided into three parts. The samples were dried at 150, 70, and 40°C (*S*1, *S*2, and *S*3) for two hours before being annealed at 900°C for three hours. The samples were subjected to X-ray diffraction (XRD) with Panalytical X'Pert Pro (model) using Cu anode as penetrating media operating under high voltage of 40 kV along with 30 mA, employed in the analysis to determine the crystalline phases as well as structural properties. The magnetic behaviors of the samples were investigated using a vibrating sample magnetometer (VSM). The microstructures were analyzed using a scanning electron microscope (SEM) with a TESCAN Vega3 (model) to view the microstructural properties for the samples dried at different temperatures.

3. Results and Discussion

This section precisely discusses the crystal lattice of different samples for the actual observation related to the impact evidenced in this experiment; analytical approach is also applied to calculate the crystallite size and strain. Lastly, the magnetic properties and morphology were clearly illustrated in detail.

3.1. X-Ray Diffraction (XRD). Figures 1 and 2 present the XRD patterns of the samples dried at different temperatures. The lattice parameters of the samples were shown in Table 1.

The amount of space occupied by $BaFe_{12}O_{19}$ and hematite (Fe_2O_3) differs, but with a nearly equal density, meaning that the mass of Fe_2O_3 magnifies the mass of $BaFe_{12}O_{19}$. When the drying temperature was 70 and 150°C, the rhombohedral shape of the Fe_2O_3 shrinks to alter the lattice parameters with a slightly loose mass, demonstrating that the volume increased without altering the density. In the case of $BaFe_{12}O_{19}$, it was discovered that there is a deviation in the lattice at the drying temperature of 70 and 150°C. The

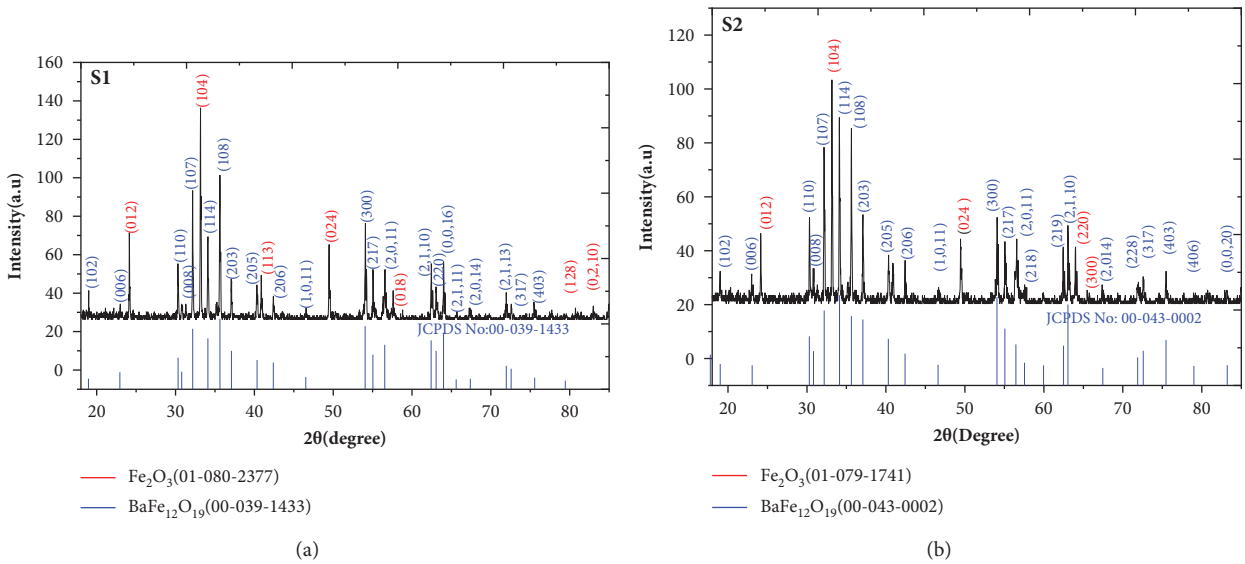

Figure 1: XRD patterns of (a and b).

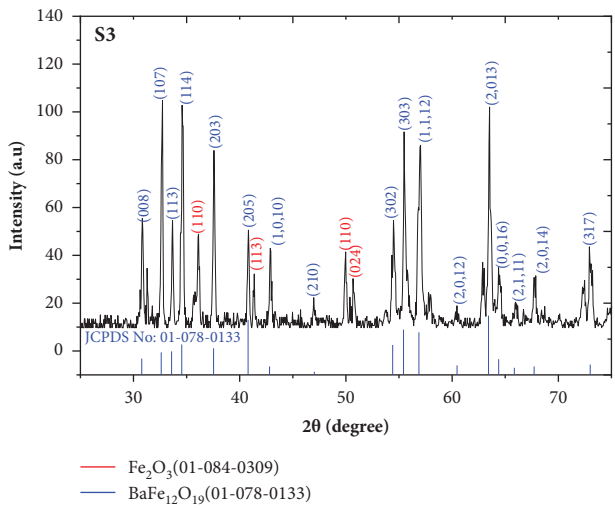

Figure 2: XRD patterns of *S*3.

hexagonal volume of the unit cell increased while the lattice constant parameters changed and the density remained constant.

Equation (1) is expressed to show the effect of change in lattice constant parameters on peaks, with miller indices due to the variation of temperatures [13]. The lattice parameters "a" and "c" as well as the wavelength (λ) at which the X-ray is exposed are constant. If these parameters are modified, the peak and miller indices will change as well.

$$\sin\theta = \sqrt{\frac{\lambda^2}{4a^2}\left[\frac{4}{3}\left(h^2 + hk + k^2\right) + \frac{l^2}{(c/a)^2}\right]}. \quad (1)$$

In fact, when these samples are exposed to X-ray, their internal molecular properties differ due to different orientations. As a result, the magnetic properties vary since the coordination of the internal molecules is oriented in different formats. X-ray is applied to a material in order to analyze its microstructural properties due to the higher energetic strength of this electromagnetic spectrum leading to penetrating the internal part of the substance. The intensity of the X-ray is reflected in different orders and at different angles (peaks). As shown in Figure 1, since the orientations are different, this resulted in different scattering. As a result, different intensities are observed from each peak. As a consequence, it is not possible to detect the same properties for a substance with different orientations.

The XRD results presented need detailed explanation. The sample *S*1 peaks are 18.94, 22.97, 30.28, 30.89, 32.23, 35.76, 37.12, 40.28, 42.5, 46.5, 54, 55.05, 56.5, 62.36, 63.1, 63.95, 65.54, 67.36, 72, 72.61, 75.54, and 79.44 in Figure 1. They correspond to the following reflections: (102), (106), (110), (108), (203), (205), (206), (1, 0, 11), (2, 0, 11), (2, 0, 14), (2, 1, 13), (3, 1, 17), and (403), and they belong to the $BaFe_{12}O_{19}$ phase with JCPDS number 00-039-1433. All these peaks are crystalline, whereas the remaining peaks have values of 24.2, 33.2, 41, 49.43, 57.5, 80.66, and 83.10. They correspond to (012), (104), (113), (024), (018), (128), and (0, 2, 10) reflections and are perfectly matched with the Fe_2O_3 phase with JCPDS number 01-080-2377.

*S*2 is similarly shown in Figure 1, comprising of $BaFe_{12}O_{19}$ and Fe_2O_3 phases recorded at different JCPDS numbers. The following peaks are matched with JCPDS number 00-043-0002, and their values are 19.06, 23.09, 30.28, 32.22, 34.07, 35.64, 37.11, 40.27, 42.48, 46.63, 54.06, 55.04, 56.50, 57.61, 59.91, 62.48, 63.09, 67.48, 71.88, 72.6, 75.41, 78.93, and 83.22. They correspond to the following reflections: (102), (006), (110), (107), (008), (114), (108), (203), (205), (206), (1, 0, 11), (300), (217), (2, 0, 11), (2, 0, 14), (228), (317), (403), (406), and (0, 0, 20). Whereas the rest of the peaks are 24.18, 33.21, 49.43, 64.06 and 65.53, these peaks are exactly matched with JCDPS number 01-079-1741 of the Fe_2O_3 phase and they correspond to the following reflections: (012), (104), (024), (220), and (300).

Table 1: The lattice parameters and density of the products.

Sample	Drying temperature (°C)	Compound	Lattice parameters (Å)	Volume (Å^3)	Density (gcm^{-3})
*S*1	150	Fe_2O_3	$a = b = 5.035$, $c = 13.751$	301.92	5.27
		$BaFe_{12}O_{19}$	$a = b = 5.895$, $c = 23.215$	698.54	5.30
*S*2	70	Fe_2O_3	$a = b = 5.034$, $c = 13.746$	301.69	5.27
		$BaFe_{12}O_{19}$	$a = b = 5.892$, $c = 23.183$	697.99	5.30
*S*3	40	Fe_2O_3	$a = b = 5.008$, $c = 13.647$	296.39	5.37
		$BaFe_{12}O_{19}$	$a = b = 5.865$, $c = 23.099$	688.11	5.36

However, Table 1 shows that *S*1 and *S*2 have the same density. Exploring out the density equivalency of *S*1 and *S*2 in the XRD results presented in Figure 1 is also important. The reflections at (114), (203), (110), (205), (108), (006), (008), and (206) are the same for *S*1 and *S*2 but with different intensities, showing that *S*2 is denser at all these reflections. Otherwise, they are almost the same at the following reflections: (1, 0, 11), (300), (217), (2, 0, 11), (2, 0, 14), (317), and (102). In the Fe_2O_3 phase, which comprises the highest intensity at (104) reflection, the portion is denser with Fe_2O_3 in *S*1 and *S*2. This shows that the density of *S*1 and *S*2 is equivalent to the result presented in Table 1.

*S*3 is presented in Figure 2, containing different sets of peaks among them, including 30.88, 32.62, 33.62, 34.53, 37.5, 40.81, 42.81, 47, 54.37, 55.56, 56.83, 60.5, 63.4, 64.38, 65.84, 67.75, and 73.03 respectively. They correspond to the following reflections (008), (107), (113), (114), (203), (205), (112), (2, 0, 12), (2, 0, 13), (0, 0, 16), (2, 1, 11), (2, 0, 14), and (317). The peaks and the reflections are found to correspond to the JCPDS number 01-078-0133 for the $BaFe_{12}O_{19}$ phase, while the other peaks are 36.17, 41.36, 50, and 50.64, which correspond to these reflections: (110), (113), (110), and (024). They are exactly matched with the JCPDS number 01-084-0309 of the Fe_2O_3 phase.

It is seen from Table 1 that the density of *S*3 is different from *S*2 and *S*3 and, simultaneously, from the XRD results presented in Figure 2, possesses different reflections and intensities compared to *S*1 and *S*2. In this sample, only three of the reflections of $BaFe_{12}O_{19}$ were the same with *S*1 and *S*2, which are listed as (114), (203), and (205) simultaneously. The intensities of these reflections are denser than *S*1 and *S*2. These reflections have the same angles or peaks as *S*1 and *S*2 but differ in intensity, which directly denotes the rate of the mass in the portion, while the rest of the reflections have different modes of peaks with higher intensity, indicating that the whole sample is denser than *S*1 and *S*2. Indeed, *S*3 is in good agreement with the results presented in Table 1.

As a result of different peak intensities, the XRD results in Figures 1 and 2 confirmed that the samples are of different types. The peak intensities of the consecutive samples are different. As a result, different phases are detected, in much the same way on the Fe_2O_3 and $BaFe_{12}O_{19}$ peaks were referenced to different JCPDS numbers. The Fe_2O_3 is among the intermediate phase when synthesizing $BaFe_{12}O_{19}$.

Annealing contributed much to the formation of the $BaFe_{12}O_{19}$ phase due to high sintering occurrence. Some of the Fe_2O_3 phase remained, and their peaks appeared with the one sintered to form $BaFe_{12}O_{19}$ whose peaks are also presented with different intensities (see Figures 1 and 2). However, the Fe_2O_3 phases are different in all samples due to different orientations. These phases are considered to be antiferromagnetic, since the magnetic dipole moments in this compound are arranged in antiparallel form.

Annealing the samples coupled the magnetic dipole moments of various compounds, causing unequal magnetic dipole moments to orient in antiparallel order due to different atomic substances and hence lead to forming $BaFe_{12}O_{19}$. As a result, magnetic flux is produced, whereas some of the Fe_2O_3 that did not sinter during the annealing process do not, leaving only $BaFe_{12}O_{19}$ to produce net magnetic flux, as illustrated in Figure 3.

The crystallite size and the strain of the samples could be calculated with the following relations [14, 15]:

$$D = \frac{\kappa\lambda}{\beta_{\text{crystal}} Cos\theta}, \tag{2}$$

$$\varepsilon = \frac{\beta_{\text{strain}}}{4 \tan \theta}. \tag{3}$$

β_{crystal} and β_{strain} are attributed to full width at half-maximum intensity for crystal as well as strain whereas D, θ, and ε are crystallite size, peak, and strain, respectively. Equation (2) is applied to calculate crystallite size when the particle size is perfectly spherical and hence strain could be involved to interfere as a result; the Stokes-Wilson formula presented in equation (3) is expressed for strain computation due to peak broadening.

3.1.1. Calculation of the Crystallite Size and Strain. The Williamson–Hall Equation is well-suited for use in analyses involving two or more phases, where the relationship between them can be revealed by measuring the magnitude of the strains; see equation (5). β_{hkl} is the width of the peak at the half-maximum intensity, θ is the peak position, ε is the strain, k is Scherer constant, λ is the wavelength, and D is the crystallite size [16].

$$\beta_{hkl} = \beta_{\text{crystal}} + \beta_{\text{strain}}. \tag{4}$$

From equations (2) and (3), β_{crystal} and β_{strain} are turned to the subject of the relation and then substituted to equation (4) and finally formatted to the following equation:

$$\beta_{hkl} \cos \theta = 4\varepsilon \sin \theta + \frac{k\lambda}{D}. \tag{5}$$

Again, when equation (5) is precisely observed, $\beta_{hkl} \cos \theta$ and $\sin \theta$ are the only varying quantities. In the detailed

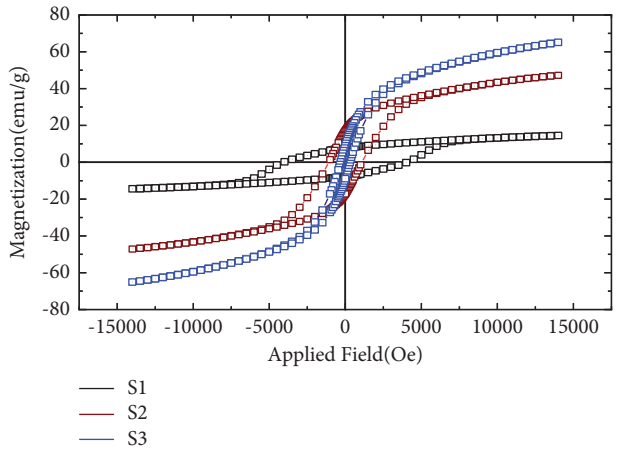

Figure 3: Hysteresis loop of samples (S1, S2 and S3).

pattern of *S*1 from Figure 1, all the peaks matched with JCPDS patterns 01-080-2377 and 00-039-1433. They are 32 peaks presented as "n". The variables quantities were calculated by taking $\beta_{hkl} \cos\theta$ as "y" and 4 $\sin\theta$ as "x", by using least square method for a linear fitting, corresponding to this formula $\overline{y} = m\overline{x} + c$. Here $\overline{y}$ and $\overline{x}$ are averages of x and y while "m" represents ε, and "c" represents $k\lambda/D$ (5). With this idea exact value of the strain and the crystallite size will be calculated. The strain and the crystallite size are given by equations (6) and (7), respectively [17]:

$$\varepsilon = \frac{n\sum_{i=1}^{n} x_i y_i - \sum_{i=1}^{n} x_i \sum_{i=1}^{n} y_i}{n\sum_{i=1}^{n} x_i^2 - \left(\sum_{i=1}^{n} x_i\right)^2}, \quad (6)$$

$$\frac{k\lambda}{D} = \frac{\sum_{i=1}^{n} y_i}{n} - \varepsilon\frac{\sum_{i=1}^{n} x_i}{n}. \quad (7)$$

The relationship between samples *S*1, *S*2, and *S*3 is shown in Figure 4. The existing differences were clearly explored showing the variation in the intercept as well as the slope. The intercept and slope were numerically calculated from equations (6) and (7), respectively. The slope was interpreted directly as strain while the intercept is the ratio of the product of Scherer constant and the wavelength to the crystallite size. The calculations were made numerically; see Tables 2 and 3.

The values presented in Table 2 are substituted to equation (6); different values of strain for *S*1, *S*2, and *S*3 were calculated and tabulated in Table 3.

Equation (7) is obtained based on the least square formula by making the intercept ($k\lambda/D$) to the subject of the relation. The ratio of the sum of "y" to "n" is the average of "y", and similarly, the ratio of the sum of "x" to "n" is the average of "x". These averages were calculated and tabulated in Table 2; using the strain (ε) calculated in equation (6), we can similarly substitute ε to equation (7) and calculate the value of $k\lambda/D$ using the average of x and y in Table 2.

It is noticed that k and λ are constants, so when these values are substituted to the value of $k\lambda/D$, the crystallite size could be calculated for *S*1, *S*2, and *S*3 which resulted in different crystallite size presented in Table 3 for different samples. The discrepancy between samples *S*1, *S*2, and *S*3 is represented analytically; it is found that samples *S*1 and *S*3 have nearly the same strain which greatly differed from *S*2 while their crystallite size varies in diminishing order of their drying temperature.

3.2. Magnetic Properties. It was shown in Figure 3 and Table 4 that the magnetic properties of the samples are diametrically opposed due to different orientations.

According to Figure 3, the magnitude by which the samples are varied is clearly identified: in sample *S*1, the coercivity is higher than samples *S*2 and *S*3. The remnant magnetization of *S*2 magnified the remnant magnetization of *S*2 and *S*3. In the hysteresis loop, this remnant magnetization indicates the rate of retentivity of a magnet in the absence of an applied magnetic field. Now, by precisely observing the samples reported in Table 4 from the hysteresis loop shown in Figure 3, the remnant magnetization significantly differed.

However, the anisotropy of the samples differs extremely, which results in producing different saturated magnetizations. With in-depth illustration, *S*1 possessed higher anisotropy, meaning the domains containing electron spins are more as compared to *S*2 and *S*3, as a consequence the domain walls are more and hence the domain wall is narrower. In this manner, the magnetic dipole moment would pass through various domains, with exchange interaction between the same and opposite poles occurring in the process. The interaction energy is high because of changes in direction across different boundaries. As a result, minimal net remnant magnetization is exhibited in *S*1.

*S*2 has less coercivity, which directly demonstrates that the anisotropy is low, as it contains fewer domains, and hence the exchange interaction is less due to the few directions by which magnetic dipole moment is transformed, which attributes in producing higher remnant magnetization. Likewise, *S*3 has less coercivity, the perturbation of magnetic dipole moments is small, and as a result minimal remnant magnetization is experienced. Indeed, the anisotropy of a magnet could be varied with drying temperature as it is simply observed in Figure 3. In this regard, the magnitude by which the anisotropies were deviated is directly proportional to the temperature.

The difference in saturated magnetization between the samples needs detailed explanation. The *S*1 has a coercivity of 4030 Oe as shown in Figure 3, which is defined as the applied field that can overcome domain wall energy by forcing the domain wall to move until a single domain is achieved. As a result, the interaction energy is reduced. Since there is no transition from domain to domain, all magnetic dipole moments remained in their respective order, resulting in saturated magnetization of 14.4 emu/g.

*S*2 can withstand any applied field less than 1080 Oe; at the 1080 Oe and above, the domain walls completely collapsed and a single domain is obtained. As a result, the interaction energy is drastically reduced because there is no transition of directions from domain to domain along the way magnetic dipole moments are rotated due to collisions

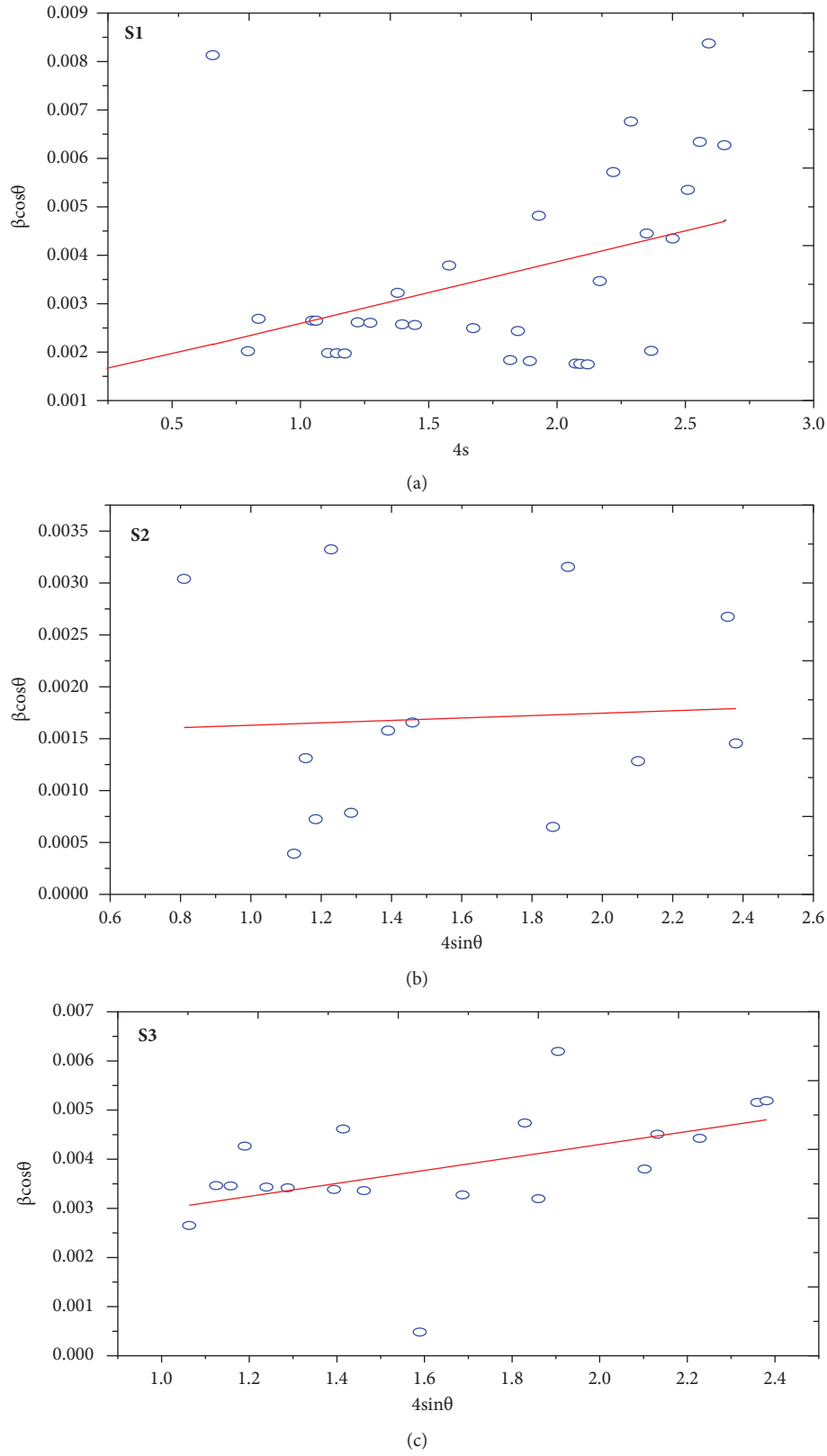

Figure 4: Williamson–Hall Plots for the samples dried at different temperatures.

Table 2: The numerical parameters of equations (3) and (4).

Sample	Drying temperature (°C)	Sum (x)	Sum (y)	Sum (x^2)	Sum (xy)	Average (x)	Average (y)
$S1$	150	55.72	0.11	108.02	0.21	1.7412172	0.0035372
$S2$	70	20.24	0.02	34.59	0.03	1.5567888	0.0016941
$S3$	40	31.41	0.07	55.41	0.13	1.6530564	0.0038419

Table 3: Crystallite size and strain of $S1$, $S2$, and $S3$.

Sample	Strain	Crystallite size (nm)
$S1$	0.00127	105.1
$S2$	0.00012	91.6
$S3$	0.00132	83.5

Table 4: The magnetic properties of samples $S1$, $S2$, and $S3$.

Sample	Drying temperature (°C)	Coercivity (Oe)	Saturated magnetization (emu/g)	Remnant magnetization (emu/g)
$S1$	150	4030	14.4	7.9
$S2$	70	1080	47	17
$S3$	40	300	65	10

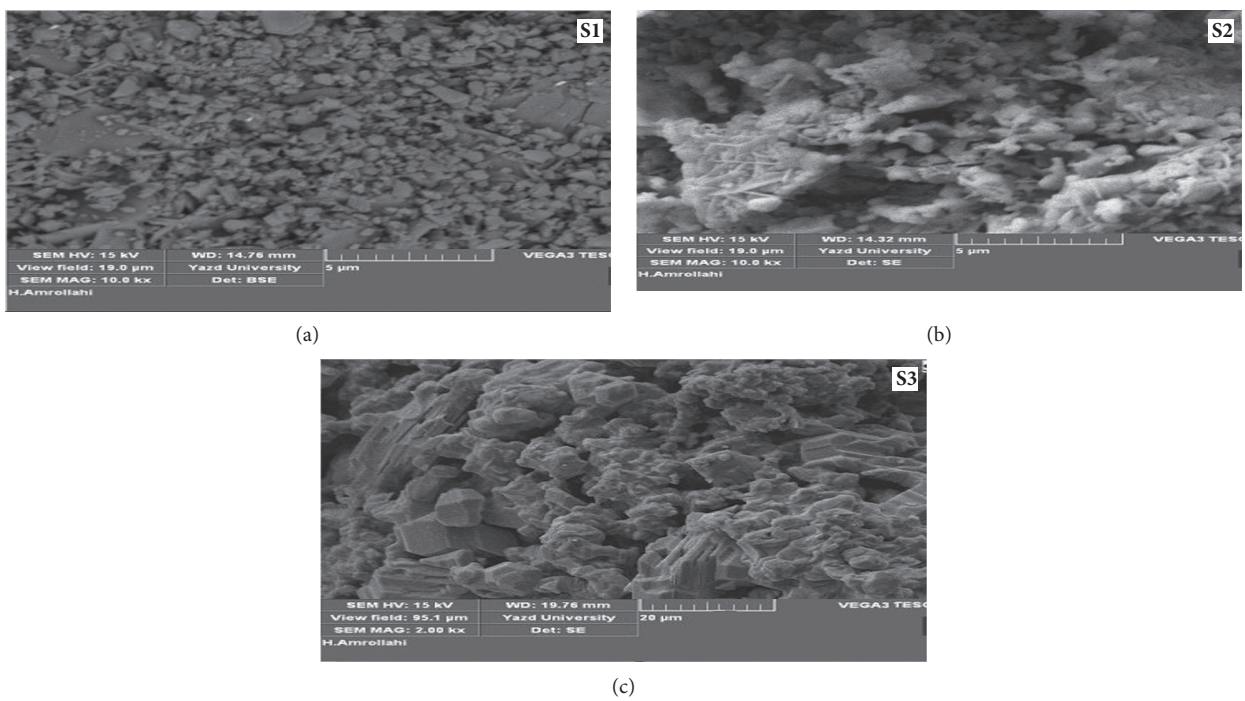

Figure 5: SEM samples (a–c).

in various boundaries. As a consequence, the saturated magnetization of 47 emu/g is formed. $S3$ has a coercivity of 300 Oe; it is the smallest applied field capable of transforming multiple domains into a single domain. It demonstrates that domain walls are few in comparison to others, but the effect of magnetocrystalline anisotropy on domain wall in this sample is extremely weak, as a small magnitude of applied field cancels all domain walls to form a high saturated magnetization of 65 emu/g.

Besides that, the sample dried at 150°C has a crystallite size of 105.12 nm (see Table 4), and it is considered as bulk materials, while the other samples dried at 70 and 40°C have crystallite size of 91.6 nm and 83.5 nm, respectively. The $S2$ and $S3$ are nanoparticles with respect to the particle size, and the spin power of these samples is 10,000 times as much as the spin of sample $S1$. As a result, higher saturated magnetization is experienced. The particle size is directly proportional to the coercivity; samples $S2$ and $S3$ behave in superferrimagnetism behaviors which resulted in forming high saturated magnetization with respect to the particle size, as witnessed in Williamson–Hall Equation analysis.

There is both positive and negative saturated magnetization in the hysteresis loop; for details see Figure 3, denoting the emission and reception of magnetic flux of a magnet. These are the saturated magnetizations that result in a single domain, after which the magnetic dipole moments are well strengthened in antiparallel form due to the exchange interaction between opposite poles. The ferrimagnetic oxide of the iron phase is synthesized from various atomic substances. As a result, magnetic flux is formed because the other phase is considered to be Fe_2O_3, which has no magnetic flux and is antiferromagnetic. The net magnetic flux is released at one end of a magnet (north pole) and ends at the other end (south pole). As a result, the saturated magnetization, the coercivity used to form this behavior, and the magnetization retained after the applied field is removed are classified as positive and negative, since the magnetic flux will be continually cycled through various poles of the magnet.

3.3. Morphology. SEM is used to define how microstructural shapes appear; the appearance of different samples is detected differently as all shapes are observed in Figure 5. The microstructural impact of each phase is different. Each phase has domain walls when it is not in saturated state. The rate of intense pinning of domain walls is attributed to the effect of magnetocrystalline anisotropy [18]. This anisotropy strictly restricts the domain walls from moving in other to attain a single domain due to the high rate of interaction. The anisotropy of the samples is directly proportional to the asymmetry of the SEM images.

In *S*1, the rate by which the anisotropy is noticed greatly differed from *S*2 and *S*3. The anisotropy of *S*1 is about 4 times greater than the anisotropy of *S*2 and about 13 times greater than the anisotropy of *S*3, since the coercivity is directly proportional to the anisotropy as it was evident in Table 4 and Figure 3, as well as the difference of the SEM images presented in Figure 5. As a result, the rise in saturated magnetization in the *S*2 and *S*3 is due to less anisotropy, which means that partial pinning results in the formation of high saturated magnetization and lower coercivity.

4. Conclusion

The intensive effort was made to explore the impact of drying temperature on the magnetic and microstructural properties of $BaFe_{12}O_{19}$. The precursors were coprecipitated. It was discovered that the alteration of drying temperature is the major factor, causing the variation of the microstructural properties as well as the magnetic properties of $BaFe_{12}O_{19}$ when the temperature is altered at mixing stages. The sample was dried at different temperatures and was treated with an identical annealing treatment. Different results were detected after reporting the final samples to XRD, VSM, and SEM. The effect of low drying temperature results in low coercivity and symmetrical SEM images whereas high drying temperature results in high coercivity and asymmetrical SEM images. It is further revealed that the high rate of interaction between domains causes strong pinning of domain walls as well as the asymmetry of the SEM images. Also, the strain and the crystallite size of the samples are different when calculated with the least square formula using the Williamson–Hall Equation in the order of varying and constant quantities. The *S*1 and *S*3 were found to have close strain and greatly differed from *S*2, but their crystallite sizes were organized in descending order of drying temperatures. The Williamson–Hall Equation is mostly used for perfect spherical shapes [19]. In this study, the hexagonal shape is approximately taken as spherical to calculate crystallite size, as hexagonal shapes cannot be directly applied to calculate crystallite size with SEM images. Otherwise, the study was carried out to largely expose the effects of drying temperature on the magnetic and microstructural properties of $BaFe_{12}O_{19}$ in the preparation process.

Data Availability

The raw data used to support the findings of this study are not included within the article. They could be given on request for further action.

Conflicts of Interest

The authors declare that they have no conflicts of interest.

Acknowledgments

The authors thank Magnetism Lab members of Yazd University for the technical and experimental system assistance.

References

[1] H. Sözeri, I. Küçük, and H. Özkan, "Improvement in magnetic properties of La substituted BaFe12O19 particles prepared with an unusually low Fe/Ba molar ratio," *Journal of Magnetism and Magnetic Materials*, vol. 323, no. 13, pp. 1799–1804, 2011.

[2] H. Sözeri, "Simple recipe to synthesize single-domain $BaFe_{12}O_{19}$ with high saturation magnetization," *Journal of Magnetism and Magnetic Materials*, vol. 321, no. 18, pp. 2717–2722, 2009.

[3] P. Kumar and A. Gaur, "Signature of multiferroicity and pyroelectricity close to room temperature in $BaFe_{12}O_{19}$ hexaferrite," *Ceramics International*, vol. 43, no. 18, pp. 16403–16407, 2017.

[4] A. Ataie and M. Montazeri-Pour, "Formation mechanism of $BaFe_{12}O_{19}$ nanoparticles processed via wet chemical route using mixed solvent," *International Journal of Nanoscience*, vol. 10, pp. 1083–1086, Article ID 04n05, 2011.

[5] F. Gao, D. Li, and S. Zhang, "Mo"ssbauer spectroscopy and chemical bonds in $BaFe_{12}O_{19}$ Hexaferrite," *Journal of Physics Condensed Matter*, vol. 15, p. 5079, 2003.

[6] S. Tyagi, V. S. Pandey, S. Goel, and A. Garg, "Synthesis and characterization of RADAR absorbing $BaFe_{12}O_{19}/NiFe_2O_4$ magnetic nanocomposite," *Integrated Ferroelectrics*, vol. 186, no. 1, pp. 25–31, 2018.

[7] R. C. Pullar, "Hexagonal ferrites: a review of the synthesis, properties and applications of hexaferrite ceramics," *Progress in Materials Science*, vol. 57, no. 7, pp. 1191–1334, 2012.

[8] V. P. Singh, R. Jasrotia, R. Kumar et al., "A current review on the synthesis and magnetic properties of M-type hexaferrites

material," *World Journal of Condensed Matter Physics*, vol. 8, no. 2, pp. 36–61, 2018.

[9] K. Habanjar, H. Shehabi, A. M. Abdallah, and R. Awad, "Effect of calcination temperature and cobalt addition on structural, optical and magnetic properties of barium hexaferrite $BaFe_{12}O_{19}$ nanoparticles," *Applied Physics A*, vol. 126, no. 6, p. 402, 2020.

[10] Z. Mosleh, P. Kameli, M. Ranjbar, and H. Salamati, "Effect of annealing temperature on structural and magnetic properties of $BaFe_{12}O_{19}$ hexaferrite nanoparticles," *Ceramics International*, vol. 40, no. 5, pp. 7279–7284, 2014.

[11] R. Yensano and S. Phokha, "Effect of ph on single phase $BaFe_{12}O_{19}$ nanoparticles and their improved magnetic properties," *Journal of Materials Science: Materials in Electronics*, vol. 31, no. 14, pp. 11764–11773, 2020.

[12] S. Balamurugan, S. P. Resmi, B. C. Brightlin, V. Sherly Arputha Kiruba, and A. Reshma, "Impact of different set of precipitants on the formation of $BaFe_{12}O_{19}$ phase nanomaterials," *Journal of Nanoscience and Nanotechnology*, vol. 20, no. 6, pp. 3486–3495, 2020.

[13] C. Suryanarayana and M. G. Norton, "X-ray diffraction: a practical approach," *Online Resource*, Plenum Press, New York, NY, USA, 1998, http://public.ebookcentral.proquest.com/choice/publicfullrecord.aspx?p=3086226.

[14] D. Dastan and N. B. Chaure, "Influence of surfactants on TiO2 nanoparticles grown by sol-gel technique," *International Journal of Machining and Machinability of Materials*, vol. 2, no. 1, pp. 21–24, 2014.

[15] A. Jafari, K. Tahani, D. Dastan et al., "Ion implantation of copper oxide thin films; statistical and experimental results," *Surfaces and Interfaces*, vol. 18, Article ID 100463, 2020.

[16] D. Nath, F. Singh, and R. Das, "X-ray diffraction analysis by Williamson-Hall, Halder-Wagner and size-strain plot methods of CdSe nanoparticles- a comparative study," *Materials Chemistry and Physics*, vol. 239, Article ID 122021, 2020.

[17] K. H. Zou, K. Tuncali, and S. G. Silverman, "Correlation and simple linear regression," *Radiology*, vol. 227, no. 3, pp. 617–628, 2003.

[18] B. Liu, H. Wang, Q. Yu et al., "Quantitative analysis of pinning-hardened intrinsic coercivity of Sm (CoFeCuZr) z (z = 7.0-7.8) high-temperature permanent magnets," *Journal of Alloys and Compounds*, vol. 872, Article ID 159622, 2021.

[19] A. Khorsand Zak, W. H. Abd Majid, M. E. Abrishami, and R. Yousefi, "X-ray analysis of ZnO nanoparticles by Williamson-Hall and size-strain plot methods," *Solid State Sciences*, vol. 13, no. 1, pp. 251–256, 2011.